Volume Rendering in Three-Dimensional Display of SPECT Images

Jerold W. Wallis and Tom R. Miller

Mallinckrodt Institute of Radiology, Washington University School of Medicine, St. Louis, Missouri

Three-dimensional display utilizing volume rendering is valuable in the display of SPECT data. Volume rendering enhances continuity of structures compared to slice display, and cine display of volume rendered images facilitates understanding of spatial relationships. Image contrast and noise characteristics were analyzed for depth-weighted maximum activity projection, a form of volume rendering proposed by the authors for "hot spot" imaging in nuclear medicine. Contrast in the rendered images was nearly equal to that in slice display, and substantially improved compared to planar images. Image noise was reduced compared to both projection and slice display. Rendered images may be generated automatically in only a few minutes following filtered backprojection, permitting routine clinical use.

J Nucl Med 1990; 31:1421–1430

$\mathbf{S}$ingle-photon emission tomography provides significantly improved image contrast by separating overlapping structures. This advantage is gained, however, at the expense of ease of interpretation of the scintigraphic study. Both the number of sagittal, coronal, and transverse slices that need to be examined and the difficulty in following structures from one slice to the next make interpretation of tomographic studies more complex than that of planar studies.

Three-dimensional rendering is the process of converting a tomographic data set into a two-dimensional image in a way that incorporates depth information and spatial relationships into the image. Ideally, the rendering process will aid in perception of overall spatial relationships and decrease the number of images that need to be viewed, while preserving all of the image features necessary for accurate interpretation. Three-dimensional rendering has been employed successfully in computed tomography (*1,2,3*) and magnetic resonance imaging (*4,5*). Nuclear medicine images provide a unique challenge in three-dimensional rendering be-

cause of relatively poor image quality due to significant Poisson noise, relatively poor spatial resolution, and the wide range of uptake of tracers within organs. In a previous study (*6*), we examined various rendering algorithms and concluded that the best technique for "hot spot" imaging in nuclear medicine is a method we call maximum activity projection. The goal of this paper is to explore in more detail the characteristics of this rendering method.

MATERIALS AND METHODS

Three-dimensional Rendering Technique

Following routine acquisition and filtered backprojection, the transaxial slices are stacked to form a cube of image data. From a chosen angle, a two-dimensional projection of the cube can be constructed by placing the maximal voxel from each column into the corresponding location in the rendered image (Fig. 1).

To enhance the three-dimensional effect, depth weighting using simulated exponential attenuation is applied before finding the maximum voxel, thus leading to the following equation:

$$I_{x,y} = \overset{64}{\underset{z=1}{M}} e^{-\mu_r z} D_{x,y,z},\qquad(1)$$

where I is the rendered image, D is the $64 \times 64 \times 64$ cube of data, μ_r is the chosen attenuation coefficient, and M is the maximum operator used to choose the greatest value along the ray undergoing reprojection. Attenuation coefficient values of 0 (i.e., no attenuation), 0.024, and 0.049 cm^{-1} were chosen to assess the effect of variation in this parameter. Maximum activity projection using these values will be referred to subsequently as Max0.0, Max0.024, and Max0.049. To further enhance the perceived three-dimensional effect, images were produced from 64 angles for subsequent cine display, giving the effect of rotation of the imaged object.

For comparison with the maximum activity method, summed projection was also performed by summing activity values along columns to form a two-dimensional image:

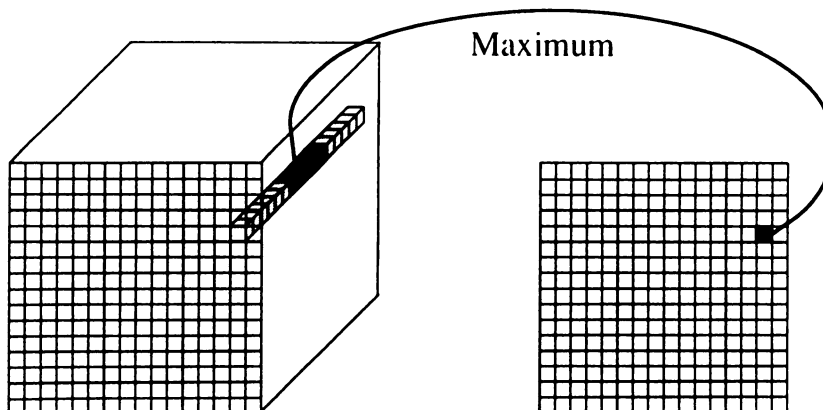$$I_{x,y} = \sum_{z=1}^{64} D_{x,y,z}.\qquad(2)$$

Implementation

The volume-rendering algorithm was implemented in FORTRAN on a microVax-II minicomputer (Digital Equipment Corp., Maynard, MA). Rotations of the reconstructed

FIGURE 1
A single ray of data is chosen from the cube of data (left), and the maximum value in the ray is placed in the corresponding location in the rendered image (right).

tomographic data were performed using bilinear interpolation with the aid of a 20 Mflop array processor (CDA/Analogic, Peabody, MA), permitting generation of 64 rendered views in 4 min.

Image Data

Patients. Selected examples are presented from clinical studies performed in our clinic. Bone scintigraphy was performed 2 hr after administration of 20 mCi of technetium-99m-(^{99m}Tc) MDP. Liver scintigraphy for hemangioma detection was performed 1.5 hr after administration of 25 mCi of ^{99m}Tc-labeled red blood cells.

Tomographic data were acquired with use of a commercially available rotating gamma camera (Siemens Gammasonics, Inc., Des Plaines, IL) using 64 angles over a 360-degree circular orbit with a total acquisition time of 30 min. A high-resolution low-energy collimator was employed. Reconstruction was performed with a ramp filter using the manufacturer-supplied software. Following reconstruction, three-dimensional filtering (7) was performed in the spatial domain with use of a Wiener filter (8).

Phantoms. To evaluate the performance of the algorithm in a setting of hot lesion detection with moderate background, as would be the case in a hemangioma or gallium study, a 22-cm diameter cylindrical phantom with hollow spherical inserts was employed (Data Spectrum Corp., Chapel Hill, NC), with acquisition and backprojection performed as described above. In addition, attenuation correction was applied using the Chang first-order correction algorithm (9). The phantom was filled with water containing 25 mCi [^{99m}Tc]pertechnetate. A hollow insert with diameter 3.1 cm or 3.8 cm was placed centrally in the phantom. The inserts were filled with a water/pertechnetate solution which had a specific activity 2.8 times the surrounding background to approximate the blood pool:liver ratio in hemangioma detection. Approximately 400,000 counts were acquired in each of the 64 views, and backprojection was performed as described above. Following reconstruction, three-dimensional filtering (7) was performed in the spatial domain with use of a Butterworth filter (order 5, cutoff .7).

To evaluate noise, images of the uniform cylindrical phantom were acquired exactly as described above, but without the spherical inserts.

Computer-Generated Lesions. To evaluate the performance of the algorithm in bone imaging, where background activity is significantly less than for hemangioma detection, lesions of

varying sizes were added to the projection images of a bone study in a normal patient. The following method was employed:

1. Lesions with sizes of 1.9 × 1.9 × 1.2 cm and 1.2 × 1.2 × 0.6 cm were positioned at locations corresponding to the normal second and fourth lumbar vertebral bodies in the reconstructed study, with a lesion intensity of ~4 times normal bone.
2. Simulated projections of the lesion were constructed from 64 angles over 360° (corresponding to the acquired projections) as follows:

    a. The cube was rotated using bilinear interpolation to each angle corresponding to the angles of acquisition of the raw data.
    b. Depth-dependent blur was added to the cube, based on voxel position and radius of rotation of the camera. Prior to the study, line spread functions were measured at multiple distances from the collimator to calculate the distance dependence of blur for this camera/collimator combination.
    c. Attenuation was applied to voxels in the cube, using the attenuation coefficient for water (μ = 0.12 cm^{-1}), with depth determined in relation to an outline of the body contour.
    d. Voxels in the cube were summed to form projection images at each angle, and Poisson noise was introduced.

3. The projection images of these simulated lesions were added to the corresponding patient images, to form "abnormal acquired data."
4. The abnormal acquired data were then reconstructed using filtered backprojection, and slices and rendered images were generated as described above. Thus the raw, slice, and rendered images used for analysis were all produced from the same projection data set.

Data Analysis

Lesion Contrast. Contrast (C) was determined using the equation:

$$C = (T - B)/B \quad (i.e., C = T/B - 1). \quad (3)$$

The counts in the target (T) were determined from the peak count value of a profile through the center of the sphere or lesion, and mean background counts (B) were determined

from a manually-drawn region adjacent to the lesion. For evaluation of simulated lesions in patient data, lesion contrast in a planar projection is dependent on viewing angle; the posterior and lateral views were chosen for analysis. Comparison regions were chosen both in soft tissue and in normal areas of the lumbar spine, and the relative activities of the lesions, normal bone and soft tissue were computed.

Noise. Analysis of noise characteristics was performed using a uniform cylindrical phantom. Noise was quantified by computing the mean ($\bar{x}$) and standard deviation (s) of the pixel values within a large central region in the image. The root mean square error (%RMS), representing the noise, is the ratio of the standard deviation (s.d.) to the mean counts: %RMS = $100 \cdot s/\bar{x}$. The %RMS noise was computed from an unfiltered planar projection, a central slice through the filtered backprojected data, and from the volume-rendered image. Exact comparison of the amount of noise present in different display modalities is difficult. The %RMS noise in a planar study is a function of the counting statistics and matrix size; in tomographic studies the reconstruction filter adds an additional variable, and in three-dimensional rendering the object size and shape are also important. While simultaneous analysis of resolution and noise could be performed under varying filter conditions, the result would still be applicable only to the size and shape of the object used for the phantom experiment. The phantom employed was therefore intended to give a rough comparison of noise characteristics with use of parameters that approximate clinical studies.

Theoretical Contrast Estimation

Consider a hypothetical phantom consisting of a sphere with diameter D and specific activity Q_s contained within a cylinder with diameter L and lesser specific activity Q_b, as shown in Figure 2.

To a first approximation, the contrast in planar imaging is a function of the relative activities $((Q_s - Q_b)/Q_b)$ and the diameters (D/L). Including contrast degradation due to finite system resolution (CF), scatter (SF), and attenuation (A) the contrast is (*10*):

$$C_{planar} = \frac{Q_s - Q_b}{Q_b} \cdot \frac{D}{L} \cdot CF \cdot \frac{1}{1 + SF} \cdot A, \qquad (4)$$
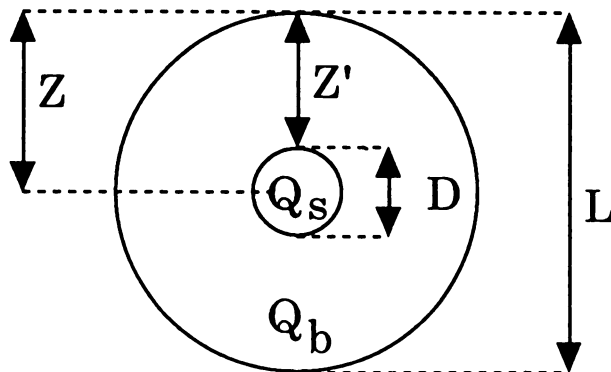

FIGURE 2
Cylindrical phantom (diameter L) with moderate background activity (Q_b) containing a spherical lesion (diameter D) with high specific activity (Q_s). The sphere is at a depth Z within the cylinder; its surface is at distance Z' from the surface of the cylinder.

where

$$A = \frac{e^{-\mu_p Z}}{[\sinh(\mu_b L/2)/(\mu_b \cdot L/2)]e^{-\mu_b L/2}}, \qquad (5)$$

and μ_p is the (narrow beam) attenuation coefficient for the sphere, μ_b is the (broad beam) effective attenuation coefficient for the background, and Z is the depth of the sphere.

In tomographic imaging, the contrast is nearly independent of sphere and cylinder diameters because specific uptake is measured and there is no superimposition of background activity. Thus, the detection of small lesions is enhanced because of the improved contrast compared to planar imaging. If attenuation compensation is employed, the contrast is also independent of lesion depth and attenuation (*10*):

$$C_{slice} = \frac{Q_s - Q_b}{Q_b} \cdot CF \cdot \frac{1}{1 + SF} \cdot \qquad (6)$$

However, because of the partial volume effect, the improvement in contrast will decline for very small lesions.

Our volume rendering method gives the same contrast as is present in tomographic slices in the absence of noise when simulated attenuation is not employed ($\mu_r = 0$ in Equation 1), as demonstrated later in the discussion section. If the images are viewed in rotating format, some degree of simulated attenuation should be added to the rendering process, as described above, to prevent the illusion of reversal of rotation during viewing (*11*). Addition of attenuation will slightly decrease the contrast in the rendered images compared to the slice data. When simulated exponential attenuation is applied, the maximum operator will detect the most anterior surfaces of the background and the sphere, as these will have the least attenuation. The counts in the sphere (T) will therefore experience greater attenuation than the background as a function of the depth of the surface of the sphere from the surface of the background (Z' in Fig. 2):

$$T_{rendered} = T_{slice} \cdot e^{-\mu_r Z'}. \qquad (7)$$

Finally, contrast in the rendered image will be slightly decreased relative to slice data when noise is added to the otherwise uniform background. Noise will produce some pixels that are higher than the mean value; it is these pixels that will be selected by the maximum operator, raising the mean value in the rendered image. This effect can be quantified by a "noise accumulation factor" (NF) that is dependent on the simulated attenuation coefficient (μ_r), image noise and object thickness, as discussed in the Appendix. The effect of NF is most significant in thicker structures, such as soft-tissue background (B), increasing the detected background value:

$$B_{rendered} = B_{slice} \cdot NF. \qquad (8)$$

Thus, the net effect of simulated attenuation and noise will be to slightly increase background and slightly decrease the detected lesion activity, resulting in a mildly decreased target:background ratio and therefore decreased contrast in the rendered images compared to the tomographic slices. Combining Equations 3, 7, and 8:

$$C_{rendered} = (C_{slice} + 1) \cdot \frac{(e^{-\mu_r Z'})}{NF} - 1. \qquad (9)$$

The exact value of NF is difficult to estimate analytically; however, based on our phantom data, NF ranges from 1 to

FIGURE 3
Volume rendering of two clinical tomographic studies, at multiple angles. Top: Bone scan with subtly increased uptake at L5-S1 following a motor vehicle accident. Bottom: Hemangioma study showing a large hepatic hemangioma. Other vascular structures in the chest and abdomen are also clearly shown.
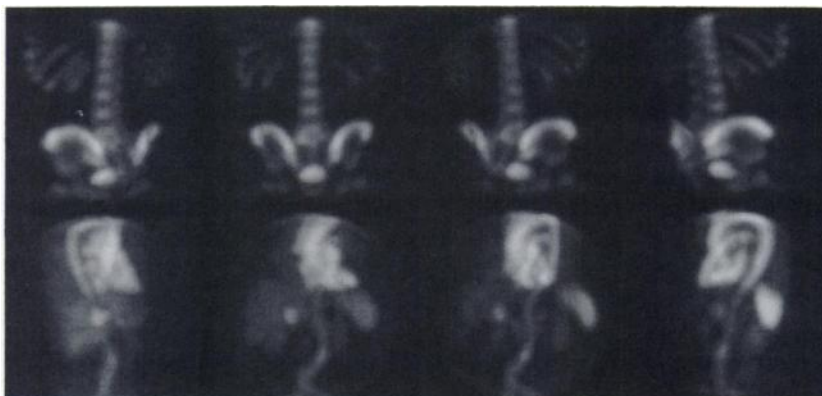
1.11 depending on object thickness, count density, and simulated attenuation. For the cylindrical phantom employed in this study, the degradation of contrast (compared to slice data) computed from Equation 9 due to simulated attenuation and noise is 19% for Max0.0, 32% for Max0.024, and 54% for Max0.049.

In the setting of a low background, as exemplified by the simulated bone abnormalities, the slight increase in soft-tissue background is not visually detectable. For the comparison of abnormal vertebral bodies with adjacent normal vertebral bodies, the similar depth of the normal and abnormal structures will cause Z' to be approximately zero. The relatively small thickness of the spine will cause NF to be near unity. Thus, lesion contrast in the rendered images should be essentially equal to that in transaxial slices.

RESULTS

Sample Images

Examples of volume rendering in clinical bone scintigraphy and hemangioma detection are shown in Figure 3. Rendered images from four angles are shown in the illustration; for clinical interpretation, images were produced from 64 angles over 360 degrees and viewed in a cine display.

Figure 4 shows a comparison of slice display, maximum activity projection, summed reprojection, and display of raw projection data for the simulated bone lesions. The coronal slice that passed through the simulated lesions in the second and fourth vertebral bodies is shown, along with the posterior raw and rendered images. Note that the lumbar spine curves into and out of the image plane on the coronal slice, thereby hindering interpretation; this problem is not present in the rendered images. Lesion contrast in the image created with maximum activity projection is approximately equal to that in slice display, and is superior to that in the summed reprojection or the noisier raw projection images, where the upper simulated lesion is not definitely perceptible.

Evaluation of Lesion Contrast

Phantom Contrast. Measured contrast values from the phantom study are shown in Figure 5 for raw, slice

and rendered image data for two lesion sizes. The rendered image contrast agrees well with the theoretical results derived above with predicted/measured results of 0.91/0.94 for Max0.0, 0.76/0.83 for Max0.024, and 0.52/0.51 for Max0.049; slight discrepancies are likely due to imperfect attenuation correction and the varying depth of the curved surface of the cylindrical phantom. Note that contrast in the images generated using maximum activity projection is much improved compared to the planar and summed images, and is nearly equal to that achieved in tomographic slices. The relatively high simulated attenuation used in Max0.049 and the combination of a centrally located lesion and considerable background represents a worst case, for this volume rendering method; even in this case, contrast is superior to that seen in planar imaging. Contrast is strongly dependent on object thickness in planar im-
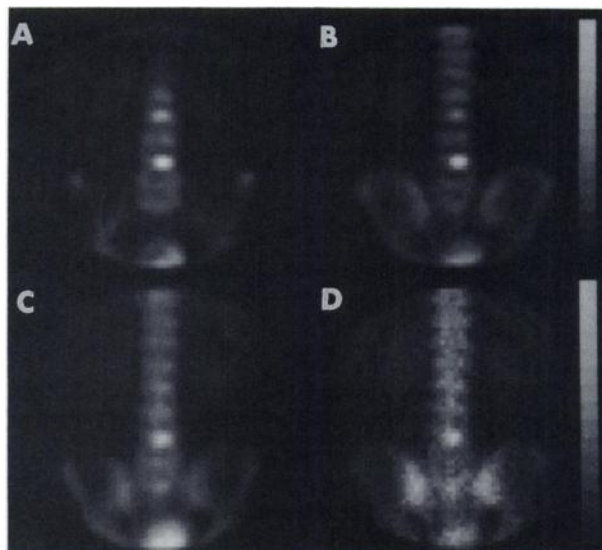

FIGURE 4
Posterior view of the lumbar spine in a normal patient following addition of two simulated lesions. The spine curves in and out of the imaging plane in the coronal slice (A); this is not the case following depth-weighted maximum activity projection (B). Lesion contrast is inferior using summed projection (C) and in the noisier raw projection image (D).
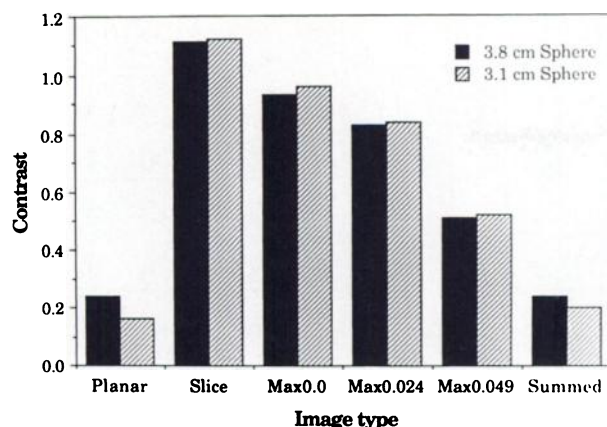
FIGURE 5
Comparison of the contrast achieved following imaging of a cylindrical phantom with hollow spherical inserts, computed from planar images, tomographic slice display, maximum activity projection, and summed projection.

aging, as shown by the planar results using two sphere sizes. This is not the case in tomographic slice data or in images created with maximum activity projection, as shown in Figure 5.

Simulated Lesion Contrast. The results of analysis of the bone scan with simulated spine lesions with rendering from the posterior view is shown in Figure 6. The ratios of lesions and background to normal bone are shown for both lesion sizes. Both the slices and rendered images demonstrate less intense uptake in the smaller lesion compared to the larger lesion, due to partial volume effect. Contrast in the rendered images is equal to that of transaxial slices, as derived previously. Lesion contrast in the rendered images from the lateral view is essentially the same as in the posterior view (mean
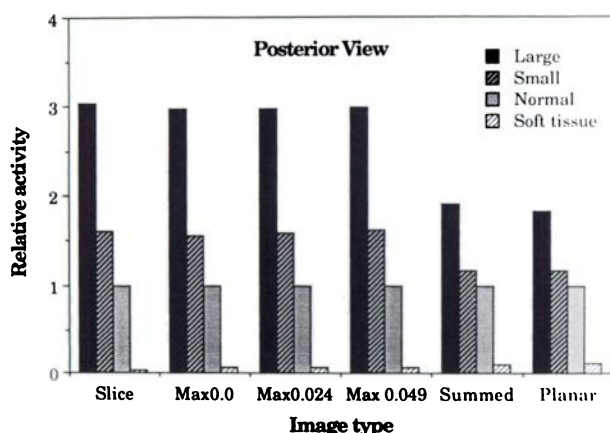

FIGURE 6
Following addition of simulated lesions to a normal bone scan, reconstruction and rendering from a posterior projection were performed using the same methods as in Figure 5. The graph depicts activity of the large and small simulated lesions and the soft-tissue background compared to normal bone, which has an arbitrarily defined activity of unity.

difference 1.0%), allowing easy identification of lesions from multiple angles during cine display.

Evaluation of Noise

Measurements of image noise yielded the following results [image type (%RMS noise)]: Slice (7.2), Max0.0 (3.7), Max0.024 (3.4), Max0.049 (3.6), and Projection (4.6). As predicted in the Appendix, noise was decreased in maximum activity projection compared to that observed in slice data. Slight variation in detected noise with change in μ_r is likely due to the irregular distribution of noise within the phantom combined with the effect of depth weighting. Noise in the volume-rendered images was less than that in the projection data, although this is partly due to the filter employed during reconstruction.

The mean detected activity in the uniform phantom was found to be 11% higher when maximum activity projection was employed without simulated attenuation than when slice data were evaluated (i.e., NF = 1.11 in Equation 8); this effect was substantially diminished (<2%) when attenuation was added.

DISCUSSION

Types of Three-Dimensional Display

Two major characteristics can be used to group the various methods of three-dimensional rendering that we and others have developed: illumination and segmentation (Table 1). Segmentation refers to the division of the image into several regions. This can be done by defining a threshold, for example separating by attenuation number all the voxels that represent bone from those that represent soft tissue in a x-ray computed tomography study. This process results in a binary image containing only the edge information. Addition of a computer-generated light source (*12*) allowed generation of shadows, thus adding substantial realism and improved surface detail to the rendered image. While segmented images have been created in nuclear medicine (*13,14*), the resultant images are heavily dependent on the threshold value, and only the surfaces of organs are displayed; information about the interior of organs is lost.

An additional disadvantage of full segmentation is the difficulty of accurate classification of voxels; erro-

TABLE 1
Types of Three-Dimensional Display

	Illuminated	Not illuminated
Full segmentation	Lighted surface display (*12, 13, 14*)	Depth-weighted surface display (*1*)
Partial or absent segmentation	Volumetric compositing (*15*)	Summed projection (*20, 21*) Maximum activity projection (*6*)

neous classification will result in the formation of an improper boundary. In addition, the limited image resolution and overlap of tissue characteristics lead to a "gray zone" in which voxels are appropriately classified not as being in one organ or another, but as having some features of both. These limitations led to the development of volume imaging (the second row in Table 1), in which information from the entire volume is incorporated into the rendered image and exact boundary determination is not performed. In volumetric compositing, ranges of voxel values are chosen to define organs, with allowance for intermediate values. The volume is then integrated into a rendered image, using lighting information to depict organ surfaces (15). Unfortunately, the resulting images are heavily dependent on the chosen intensity ranges (6), and only organ surfaces are portrayed.

It is only when no segmentation or illumination is employed (the lower right category in Table 1) that activity is portrayed without use of arbitrary thresholds. Of the possible methods in this category, we propose the use of maximum activity projection to enhance contrast for "hot spot" imaging in nuclear medicine (6, 22). Unlike techniques based on illumination, maximum activity projection leads to a rendered image reflecting relative uptake of tracer, a characteristic essential for accurate interpretation of scintigrams. The absence of user-selected parameters ensures reproducibility of the rendering process. The production of rendered images from multiple angles with subsequent cine display imparts substantial three-dimensional effect at the time of image viewing. Cine displays of raw projection data have previously been found useful in interpretation of tomographic studies (16), although poor contrast and high noise limit the utility of this display. Volume rendering allows the generation of a cine display with enhanced contrast in which each image contains counts from the entire data collection, resulting in improved image quality.

Characteristics of Maximum Activity Projection

Volume rendering using maximum activity projection has several of the desirable characteristics of planar imaging; overall spatial relationships are easily perceived and image information can be rapidly assimilated by the viewer. In addition, as demonstrated above (Fig. 4–6), image contrast in the rendered images is substantially improved compared to planar studies, with contrast approaching that achieved in tomographic slices. The mechanism for the improved contrast using maximum activity projection compared to both planar imaging and summed projection is apparent from Figure 7. In summed projection, the thickness of the overlying background results in a cumulative activity that reduces contrast; the situation in planar imaging is quite similar (Fig. 7A). In maximum activity projection,
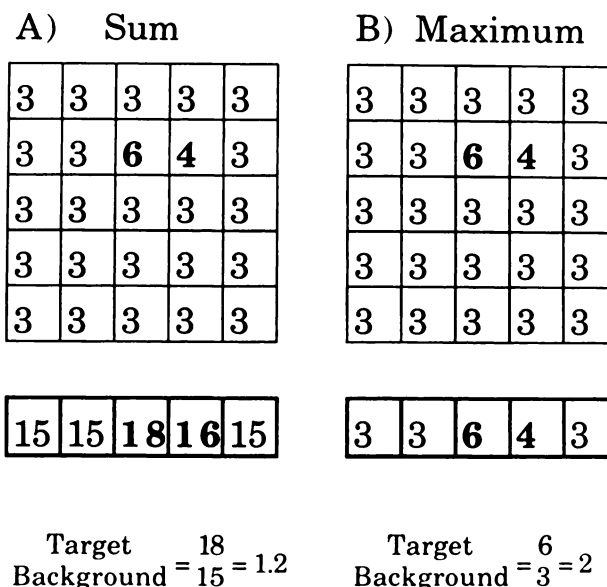
A) Sum

3	3	3	3	3
3	3	**6**	**4**	3
3	3	3	3	3
3	3	3	3	3
3	3	3	3	3

15	15	**18**	**16**	15

B) Maximum

3	3	3	3	3
3	3	**6**	**4**	3
3	3	3	3	3
3	3	3	3	3
3	3	3	3	3

3	3	**6**	**4**	3

$$\frac{\text{Target}}{\text{Background}} = \frac{18}{15} = 1.2 \qquad \frac{\text{Target}}{\text{Background}} = \frac{6}{3} = 2$$

FIGURE 7
Top: Hypothetical tomographic slice containing an area of increased activity surrounded by uniform background. Bottom: Effect of rendering by summing along columns (A) and by using maximum activity projection (B).

the contrast available in the tomographic slice is preserved for imaging of areas of increased activity (Fig. 7B).

Noise amplification during reconstruction hinders interpretation of tomographic slices, despite the use of carefully constructed low-pass filters. Volume rendering using maximum activity projection results in decreased image noise compared to both slice data and raw projection images. Summed reprojection would decrease noise as well, but at the expense of image contrast.

Some degree of simulated attenuation is needed to prevent the illusion of reversal of the direction of rotation during cine display of rendered images (11). Attenuation also serves to prevent structures far from the viewing plane from interfering with the assessment of closer structures. In the setting of low background, such as bone scintigraphy, the choice of attenuation coefficient is not critical, since lesion contrast compared to normal structures at the same depth is essentially independent of the chosen value. We have found empirically that an attenuation coefficient of 0.049 cm^{-1} is useful both in preventing image reversal and in aiding the assessment of closer structures during rotating cine display. In the setting of a higher background, such as the detection of hemangiomas within the liver, higher contrast will be obtained if the minimum amount of simulated attenuation is added during rendering. An attenuation coefficient value of 0.024 cm^{-1} can be used in this setting; however using this lower value also lessens the desirable characteristics of attenuation, noted above. In the setting of a relatively high background, it is also important to perform attenuation

correction during tomographic reconstruction. Lack of attenuation correction would result in decreased image contrast in the rendered images, and may obscure deeper lesions.

When three-dimensional images are used to aid study interpretation, it is important to be aware of the limitations of the rendering process. Areas of decreased uptake will not be shown by maximum activity projection. Similarly, in the case of mildly increased uptake centrally with more intense peripheral uptake (e.g., an abnormal pertechnetate brain scintigram or a tumor with necrotic center), the central activity will not be visible using this algorithm. While this technique is quite valuable in hot spot display, its limitations suggest that it should supplement rather than replace conventional slice display.

CONCLUSION

Volume rendering using depth-weighted maximum activity projection has been shown to combine many of the desirable characteristics of both planar and tomographic slice imaging for detection of abnormalities with increased uptake. The excellent display of overall spatial relationships inherent in planar imaging is preserved or enhanced, and the high contrast of slice data is retained, but with reduced noise. These attributes of this new display method aid in the evaluation of tomographic slices and have made viewing of volume-rendered images an essential part of the interpretation of SPECT studies at our institution.

APPENDIX

Theoretical Noise Evaluation

The expected noise in planar and tomographic imaging has been well described (17,18). The noise within a uniform object in a volume-rendered image will be similar to that in the slice data, with an additional term dependent on the object thickness in voxels. In the examination of measured activity in tomographic slices, the distribution $S(x,m)$ describes the probability of obtaining the value x when the true value is m. For a uniform object n pixels thick, the distribution $P(x,m,n)$ following maximal voxel projection may be thought of as the probability that one of the n voxels has the value x, given by $n \cdot S(x,m)$, multiplied by a term representing the probability that all other $n-1$ voxels have a lesser value:

$$P(x,m,n) = n \cdot S(x,m) \cdot \left(\sum_{i=0}^{x} S(i,m) \right)^{n-1} . \quad (10)$$

A more rigorous derivation may be produced using order statistics (19). Note that the mean value of the distribution P may be higher than the mean (m) of the original distribution, resulting in an increased detected
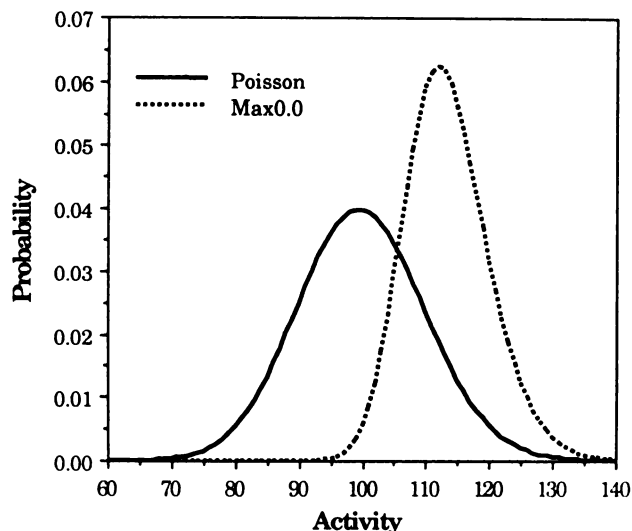

FIGURE 8
If activity in a uniform object 7 voxels thick has a mean value of 100 with Poisson noise (solid line), when maximum activity projection is performed the resulting distribution will be narrower with a higher mean (dashed line).

value quantified by the noise accumulation factor (NF) mentioned previously.

For a Poisson distribution with mean λ, the distribution following maximum activity projection is therefore:

$$P(x,\lambda,n) = n \cdot \frac{\lambda^x e^{-\lambda}}{x!} \cdot \left(\sum_{i=0}^{x} \frac{\lambda^i e^{-\lambda}}{i!} \right)^{n-1} . \quad (11)$$

As an example, this distribution for mean 100, and thickness 7 voxels is shown in Figure 8. It can be seen that the net effect of maximum activity projection is to decrease the width of the distribution (decreasing image noise) and to shift the distribution to the right, thereby slightly increasing mean image counts. In this example, the combination of noise and maximum activity projection increased the mean value by 13%; hypothetical soft-tissue background with this thickness and distribution would therefore result in a value of 1.13 for NF in Equation 8. In the case of small target lesions, n will approach unity in Equation 11, and the distribution will therefore have the same mean as the distribution in the tomographic slices; this results in an NF of unity, justifying omitting NF from Equation 7.

ACKNOWLEDGMENT

REFERENCES

1. Vannier MW, Marsh JL, Warren JO. Three-dimensional CT reconstruction for craniofacial surgical planning and evaluation. *Radiology* 1984; 150:179–184.
2. Fishman EK, Drebin B, Magid D, Scott WW, Ney DR, Brooker AF, et al. Volumetric rendering techniques: appli-

cations for three-dimensional imaging of the hip. *Radiology* 1987; 163:737–738.

3. Totty WG, Vannier MW. Analysis of complex musculoskeletal anatomy using three-dimensional surface reconstruction. *Radiology* 1984; 150:173–177.

4. Vannier MW, Gronemeyer S, Gutierrez FR, Canter CE, Laschinger JC, Knapp RH. Three-dimensional magnetic resonance imaging of congenital heart disease. *Radiographics* 1988; 8(5):857–871.

5. Axel L, Herman GT, Udupa JK, Bottomley PA, Edelstein WA. Three-dimensional display of nuclear magnetic resonance (NMR) cardiovascular images. *J Comput Assist Tomogr* 1983; 7:172–4.

6. Wallis JW, Miller TR, Lerner CA, Kleerup EC. Three-dimensional display in nuclear medicine. *IEEE Trans Med Imaging* 1989; 8:297–303.

7. Miller TR, Wallis JW, Wilson AD. Interactive reconstruction in single photon tomography. *Eur J Nucl Med* 1989; 15:189–193.

8. Miller TR, Goldman KJ, Epstein DM, Biello DR, Sampathkumaran KS, Kumar B, et al. Improved interpretation of gated cardiac images by use of digital filters. *Radiology* 1984; 152:795–800.

9. Chang LT. A method for attenuation correction in radionuclide computed tomography. *IEEE Trans Nuc Sci* 1978; NS-25(1):638–643.

10. Jaszczak RJ, Whitehead FR, Lim CB, Coleman RE. Lesion detection with single-photon emission computed tomography (SPECT) compared with conventional imaging. *J Nucl Med* 1982; 23:97–102.

11. Foley JD, Van Dam A. *Fundamentals of interactive computer graphics.* Reading, MA: Addison-Wesley; 1982:545.

12. Phong BT. Illumination for computer generated pictures. *Comm of the ACM* 1975; 18:311–317.

13. Webb S, Ott RJ, Flower MA, McCready VR, Meller S. Three-dimensional display of data obtained by single photon emission computed tomography. *Br J Radiol* 1987; 60(714):557–62.

14. Gibson CJ. Interactive display of three-dimensional radionuclide distributions. *Nucl Med Comm* 1986; 7:475–87.

15. Levoy M. Volume rendering: display of surfaces from volume rendered data. *IEEE Computer Graphics and Applications* 1988; (May):29–37.

16. Kalff V, Satterlee W, Harkness BA, Singer D, Keyes JW. Liver-spleen studies with the rotating gamma camera. *Radiology* 1984; 153:533–536.

17. Jaszczak RJ, Coleman RE, Whitehead FR. Physical factors affecting quantitative measurements using camera-based single photon emission computed tomography (SPECT). *IEEE Trans Nucl Sci* 1981; NS-28:69–80.

18. Moore SC, Kijewski MF, Muller SP, Holman BL. SPECT image noise power: effects of nonstationary projection noise and attenuation compensation. *J Nucl Med* 1988; 29:1704–9.

19. Hoel PG, Port SC, Stone CJ. *Introduction to probability theory.* Boston: Houghton Mifflin Co.; 1971:161.

20. Harris LD, Robb RA, Yuen TS, Ritman EL. Non-invasive numerical dissection and display of anatomic structure using computerized x-ray tomography. *Proc SPIE* 1978; 152:10–18.

21. Goris ML, Boudier S, Briandet PA. Interrogation and display of single photon emission tomography data as inherently volume data. *Am J Physiol Imaging* 1986; 1:168–80.

22. Miller TR, Wallis JW. Three-dimensional display of gated cardiac gated blood-pool studies. *J Nucl Med* 1989; 30:2036–41.

Editorial: Three-Dimensional Display of SPECT Images: Advantages and Problems

Modern rotating camera SPECT systems routinely generate three-dimensional image sets that contain up to 2,097,152 voxels. Since I became interested in SPECT imaging many years ago, I have been fond of posing the question, "What do I do with all this data?" The article by Wallis and Miller in this issue (*1*) addresses one answer to this question.

For many years, the approach to displaying SPECT, and indeed all tomographic images, has been to review a set of serial images in a single transaxial tomographic plane. Advances in computer displays and imaging processing have allowed the simultaneous display of images in multiple tomographic planes, usually the three orthogonal planes—transaxial, coronal, and sag-

ittal—with reference marks to indicate how the three images relate to one another. Although the use of multiple simultaneous orthogonal views implicitly recognizes the 3-D nature of SPECT images and allows the viewer to interrogate the 3-D data set directly, it does not address the problem of displaying the data as a 3-D whole. The viewer must still integrate the multiple planar tomograms into a "mental" 3-D image. Sometimes this is easy, and practice helps. Sometimes, however, when the anatomy is complicated and/or distorted by disease, it may be almost impossible to visualize what is happening in three dimensions. The problem is further complicated because a SPECT image set viewed in all three orthogonal planes may contain several hundred individual images.

The potential value of a 3-D display system for SPECT images is thus obvious. Just what such a system should be and do is still poorly defined. In order to understand the problems in designing a 3-D display